Check for updates

RESEARCH ARTICLE

ADVANCED ELECTRONIC MATERIALS
Open Access
www.advelectronicmat.de

Exploration of Chemical Composition of In–Ga–Zn–O System via PEALD Technique for Optimal Physical and Electrical Properties

TaeHyun Hong, Yoon-Seo Kim, Su-Hwan Choi, Jun Hyung Lim, and Jin-Seong Park**

In–Ga–Zn–O (IGZO) material has been researched due to its favorable electrical characteristics for application in thin-film transistor (TFT) applications such as low off current and relatively high mobility. However, most recently, as the developing and expanding application fields, conventional IGZO is a challenging aspect because higher mobility and excellent step-coverage are required to be applied to high-resolution displays and 3D NAND. In this regard, atomic layer deposition (ALD) is suggested as a novel deposition method for tackling issues. Here, this work systematically synthesizes IGZO films with various compositions by the supercycle technique of plasma-enhanced ALD (PEALD) to determine the optimum metal cation composition range of the IGZO system for high-mobility TFTs. The trends in the metal composition dependent electrical properties of ALD processed IGZO films are comparable to the previously reported results, while the structural properties are exclusive. Since both microstructure and carrier concentration affect to device characteristics complexly, the optimal In–Ga–Zn region is newly demonstrated via PEALD (X_{In}: 0.56–0.63, X_{Ga}: 0.13–0.17, X_{Zn}: 0.17–0.34). In this region, the device exhibits a remarkably high μ_{FE} of 41.4–43.7 cm^2 V^{-1} s^{-1}, a low subthreshold swing (SS) of 0.24–0.25 V decade^{-1}, an initial threshold voltage (V_{th}) of –0.9 to –1.0 V, and a slight V_{th} shift (0.01 V) under the positive bias temperature stability (PBTS).

T. Hong, Y.-S. Kim, J.-S. Park
Division of Materials Science and Engineering
Hanyang University
222, Wangsimni-ro, Seongdong-gu, Seoul 04763, Republic of Korea
E-mail: jsparklime@hanyang.ac.kr

S.-H. Choi, J.-S. Park
Division of Nanoscale Semiconductor Engineering
Hanyang University
222, Wangsimni-ro, Seongdong-gu, Seoul 04763, Republic of Korea

J. H. Lim
R&D Center
Samsung Display
Yongin 17113, Republic of Korea
E-mail: lanosjh.lim@samsung.com

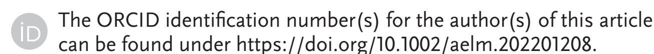
The ORCID identification number(s) for the author(s) of this article can be found under https://doi.org/10.1002/aelm.202201208.

© 2023 The Authors. Advanced Electronic Materials published by Wiley-VCH GmbH. This is an open access article under the terms of the Creative Commons Attribution License, which permits use, distribution and reproduction in any medium, provided the original work is properly cited.

DOI: 10.1002/aelm.202201208

1. Introduction

Since Hosono's group reported that an amorphous In–Ga–Zn–O (IGZO) has semiconducting behavior,[1] many studies have reported various applications of this material such as the thin-film transistor (TFT) backplane of the display,[2] 3D NAND flash memory (3D-NAND),[3] and complementary metal–oxide–semiconductor (CMOS) image sensors[4] due to their attractive advantages including low off current, a relatively low process temperature, large area uniformity, and cost effective fabrication techniques.

To understand the roles of metal components in the oxide semiconductor, many researchers have tried to design cationic species (metal components) using physical vapor deposition such as combinatorial sputtering,[5–8] solution,[9,10] and pulsed laser deposition (PLD).[11] However, in previous studies, most discussions were conducted with only a few points in the ternary phase diagram because it was difficult to control the whole region of the metal composition ratio (especially the sputtering method requires a different target each time to control the composition ratio). Alternatively, a study has been conducted in a binary metal oxide system such as InGaO (IGO).[12] According to their studies, the roles of the metal cations were quite simple. Indium (In) allows for the high mobility that is driven by the overlapping of its large spherical 5s orbitals. Gallium (Ga) can restrain free carrier generation due to strong oxygen binding energy, and zinc (Zn) acts as stabilizer for the amorphous structure.[13] Numerous sputter-processed IGZO studies showed the robust electrical TFT performances for as-deposited films and/or sputter targets with a In:Ga:Zn = 1:1:1 metal composition ratio.[14–17] Therefore, amorphous IGZO with that composition ratio has become a standard active layer deposited by a sputtering technique in the field of displays and electronics.

Recently, however, the oxide semiconductors are required controllability of film thickness accurately and chemical composition, as well as higher mobility, compared to conventional-IGZO for apply to high-end applications such as high-resolution displays using scaled down TFTs and 3D-NAND. To enhance the mobility of oxide semiconductors, many research groups have investigated the deposition of hetero- and/or

2199160x, 0, Downloaded from https://onlinelibrary.wiley.com/doi/10.1002/aelm.202201208 by Hanyang University Library, Wiley Online Library on [09/03/2023]. See the Terms and Conditions (https://onlinelibrary.wiley.com/terms-and-conditions) on Wiley Online Library for rules of use; OA articles are governed by the applicable Creative Commons License

2199160x, 0, Downloaded from https://onlinelibrary.wiley.com/doi/10.1002/aelm.202201208 by Hanyang University Library, Wiley Online Library on [09/03/2023]. See the Terms and Conditions (https://onlinelibrary.wiley.com/terms-and-conditions) on Wiley Online Library for rules of use; OA articles are governed by the applicable Creative Commons License

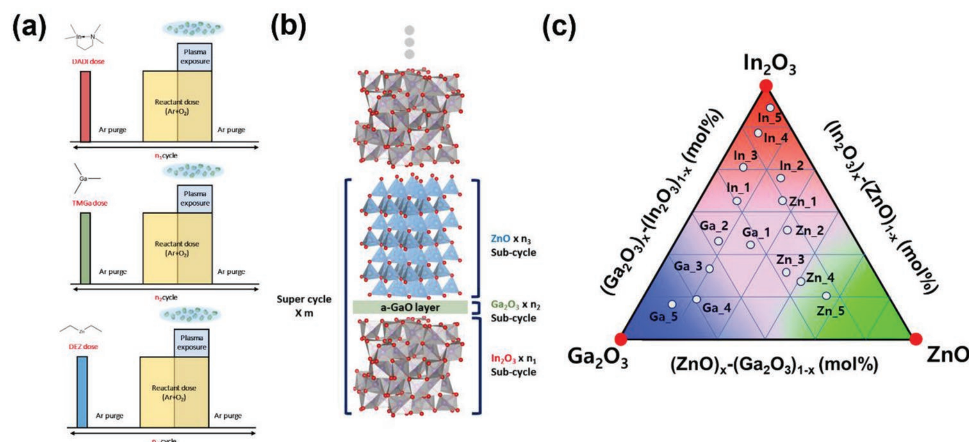

Figure 1. a) PEALD process for In_2O_3, Ga_2O_3, and ZnO using DADI, TMGa, and DEZ precursors, respectively. b) Schematic diagram of the structure of PEALD IGZO grown using sequential supercycles. c) Ternary metal oxide phase diagram of as-deposited IGZO system via PEALD

multiactive layers using sputtering.[18,19] However, this method is also difficult to control the few nanometer (nm) thickness of each layer as well as metal cation composition due to limitations of sputtering targets. Besides, sidewall engineering with stacking of each functional layers is an essential technology to realize a 3D architecture device.[20–22]

In this point of view, conventional sputtering has a drawback of step coverage because atoms and/or molecules from sputtering targets are directionally deposited. Atomic layer deposition (ALD) is considered to be a promising deposition technique to enhance electrical properties and step-coverage due to self-limiting reactions on the surface of the substrate. Because of these advantages, there are several attempts to demonstrate various semiconducting oxide materials deposited by ALD. In a previous study, we successfully fabricated the InO_x TFT deposited by ALD and achieved an electrical mobility of 16.6 $cm^2\ V^{-1}\ s^{-1}$.[23] For binary oxide systems, mobilities of indium zinc oxide (IZO)[24] and indium gallium oxide (IGO)[25] TFTs were reported to be 42.1 and 9.5 $cm^2\ V^{-1}\ s^{-1}$. In addition, a few studies for IGZO composition system have been reported to improve TFT mobility (14.8–48.3 $cm^2\ V^{-1}\ s^{-1}$).[26–28]

Generally, it is known that thermal ALD is difficult for the deposition of multicomponent films due to unexpected chemical reaction via multiple precursors, which can involve complex surface thermodynamics and kinetics reactions by differences in the vapor pressure of multimetal precursors.[24,25] These unexpected reactions are difficult to control the multicomponent composition and thickness of as-deposited oxide films. To overcome these drawbacks of thermal ALD, several researchers have introduced plasma-enhanced ALD (PEALD) to the synthesis of multicomponent oxide films. In particular, the PEALD can deposit at relatively lower temperatures due to the efficient control of the energy for reactions by controlling plasma power or time to adjust thin-film growth and characteristics compared to thermal ALD. To enhance the device electrical performance (e.g., device mobility and stability), there are remarkable studies on multicomponent oxide-based TFTs deposited by PEALD supercycle technology. Our group reported that the IGO[29] and IGZO[30] tried to control metal cation composition using by varying the subcycle in the supercycle technique of PEALD. We showed a high mobility in IGZO-based TFTs (42.1 $cm^2\ V^{-1}\ s^{-1}$) deposited at low processing temperature on a flexible substrate. However, most studies of IGZO synthesized by ALD dealt with the limited range of chemical composition, and further study is needed in the actual wide composition range in an IGZO system.

In this study, we systematically synthesized various composition IGZO films to investigate the appropriate composition range of IGZO system using a sequential deposition technique of PEALD, which have each metal cation with a tie-line of the composition ratio on In–Ga–Zn phase diagram. In addition, we evaluated the change of microstructure and composition of as-deposited films. Distinctive crystal structures were observed in the IGZO system using PEALD, which could affect thin-film properties as well as device characteristics. Since the crystal structure according to metal composition is a remarkable result of PEALD that does not report in previous sputtering[5–8] or solution methods,[9,10] we discussed it in conjunction with other properties including device characteristics and reliability.[31] Finally, staggered bottom gate IGZO TFTs were fabricated to interpret the relationship between thin-film devices, and we explored the composition ratio to optimize device characteristics.

2. Results and Discussion

To synthesize a multicomponent IGZO thin film by PEALD using a supercycle technique (**Figure 1**a), we optimized the supercycle deposition conditions by evaluating the film growth rate during each single metal oxide cycle. In our previous reports of IGZO deposited by ALD, the precursors of each single oxide layers were DADI, TMGa, and DEZ, in addition to Ar/O_2 plasma as a reactant.[30] The effect of each precursor dose and growth temperature on growth per cycle (GPC) was investigated, as summarized in Figure S1 (Supporting Information). By investigating these process conditions, we found the required growth temperature to deposit IGZO, and the PEALD process

 © 2023 The Authors. Advanced Electronic Materials published by Wiley-VCH GmbH

was conducted at a deposition temperature of 200 °C. The repetitive supercycle ALD technique sequentially divided among cubic-In_2O_3,[23,32,33] amorphous-Ga_2O_3,[34–36] and hexagonal-ZnO[37–39] was used to deposit multicomponent oxide IGZO, as presented in Figure 1b. We controlled the chemical composition of the IGZO films by adjusting the number of deposition cycles for In_2O_3, Ga_2O_3, and ZnO layer subcycles. To investigate the chemical composition of as-deposited IGZO films, XPS analysis was conducted and is summarized in Table S1 (Supporting Information). To indicate the cation atomic fraction of IGZO, we used X_i, where i is In, Ga, and Zn ($X_{In} + X_{Ga} + X_{Zn} = 1$). XPS results confirmed that all the as-deposited PEALD IGZO films were carbon-free or under limited resolution for XPS analysis, which is probably due to the higher reactivity of plasma reactants compared to other reactants such as H_2O, H_2O_2, and O_3.

Hereafter, we denote each sample as follows to make it relatively easy to recognize the amount of each component: IGZO-In # (number: 1 to 5), IGZO-Ga # (number: 1 to 5), IGZO-Zn # (number: 1 to 5) (an increase in the number means that element ratio is increased) as shown in the ternary oxide diagram of the IGZO system (Figure 1c). It is noted that the analyzed composition of $In_xGa_yZn_zO$ could be different from the designed compositions because of the nucleation effect induced by different functional ligands of each metal precursor.[29] Each XPS spectra was presented in Figure S3a–e (Supporting Information), and the intensity of metal spectra was different due to different composition ratio of thin film. The XPS O1s spectra were investigated for oxygen binding state according to In–Ga–Zn systems in PEALD IGZO (Figure S3e, Supporting Information). Each XPS O1s spectra exhibited similar properties, and it seems to have a similar behavior of oxygen during the chemical reaction under the same Ar/O_2 plasma condition. XPS depth profiles of as-deposited IGZO films exhibited a homogeneous chemical distribution and designed composition in the whole region of the vertical direction of as-deposited layers for the various composition regions as shown in Figure S3f–j (Supporting Information).

To evaluate the effect of metal composition on the optical and electrical properties of as-deposited films, the optical bandgap (E_g) and carrier concentration (N_e) were extracted by Tauc-plot methods and Hall measurements, respectively, as presented in **Figure 2**a,b. Among them, we selected the chemical composition species on two tie-lines, Line 1 (L_1, In:Ga:Zn = x:3.3:1.0) and Line 2 (L_2, In:Ga:Zn = y:1.0:1.7) and observed the characteristics of each metal composition. The bottom points of the L_1 indicate a relatively Ga-rich composition (Ga_2, Ga_3, Ga_4). However, as it goes up to the top of the line (In_1, In_3, In_4), the as-deposited films have an In-rich composition. Similarly, L_2 is the line that traverses Zn-rich (Zn_1, Zn_2, Zn_4) and In-rich (In_2, In_5) regions. In the cases of the L_1 system, the E_g values of Ga_4 and In_4 were significantly different from 4.47 to 3.34 eV. Conversely, the L_2 has generally comparable values ranging from 3.58 to 3.32 eV for Zn_4 to In_5. We inferred that the Ga fraction significantly impacted the E_g of the as-deposited films. Since the Ga_2O_3 (≈4.95 eV)[34] is generally reported as a material with a wider bandgap compared to In_2O_3 (≈3.6 eV)[32] and ZnO (≈3.27 eV),[40] we hypothesized that the E_g of the PEALD would follow the composition of each single component metal oxide. Interestingly, the E_g of the film with In:Ga:Zn = 1:1:1 was higher than that of sputter processed IGZO (≈3.2 eV). This was attributed to a higher film density when depositing using the ALD method.[27,30]

Additionally, the maps of the N_e on both L_1 and L_2 cases show that the electrical conductivity increases as the composition approaches In_2O_3 (as increasing In content). At the same time, the carrier suppression effect by Ga fraction was significant. This compositional behavior is also well explained because In_2O_3 thin films are generally reported to be conducting oxide materials, and the Ga element is well known to suppress carrier concentration. Recently, we reported that sufficient N_e (>10^{17} cm^{-3}) is a crucial property for high mobility as it can overcome the carrier transport barrier in PEALD IGZO.[30] As shown in Figure 2b, the region of appropriate N_e (>10^{17} cm^{-3}) for the potential of high mobility is above 0.306 and 0.215 of X_{In} fraction on L_1 and L_2, respectively.

We performed X-ray diffraction (XRD) for the as-deposited films with the same composition as Figure 2 to evaluate the crystallinity of IGZO films deposited by PEALD, as shown in **Figure 3**a. These results are quite different from those of the previous results of IGZO-based films, which generally showed that IGZO films with a relatively large composition region have an amorphous structure due to the different metal ionic sizes and charges (the so called, "aliovalent effect"). Hosono's group also reported an amorphous structure in a fairly large compositional area of PLD processed In–Ga–Zn system.[13] In addition, it has been reported that an amorphous phase has appeared even in not only other sputtering studies[7,8] but also

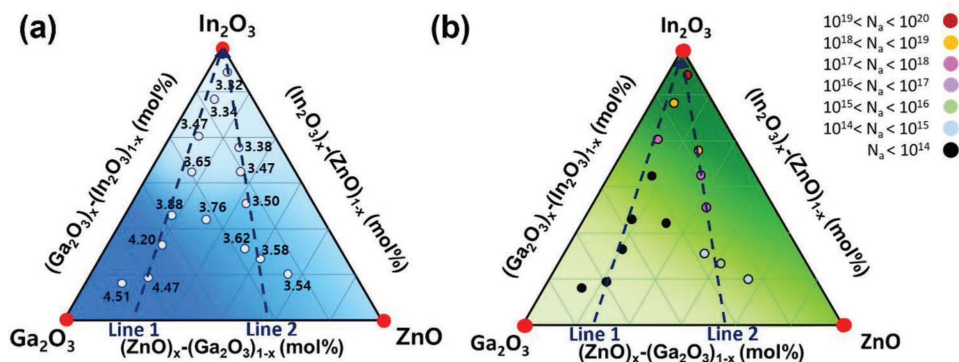

Figure 2. a,b) Ternary cation oxide phase diagrams composed of In, Ga, and Zn according to optical bandgap (a) and carrier concentration (b).

© 2023 The Authors. Advanced Electronic Materials published by Wiley-VCH GmbH

2199160x, 0, Downloaded from https://onlinelibrary.wiley.com/doi/10.1002/aelm.202201208 by Hanyang University Library, Wiley Online Library on [09/03/2023]. See the Terms and Conditions (https://onlinelibrary.wiley.com/terms-and-conditions) on Wiley Online Library for rules of use; OA articles are governed by the applicable Creative Commons License

ADVANCED ELECTRONIC MATERIALS
Open Access
www.advelectronicmat.de

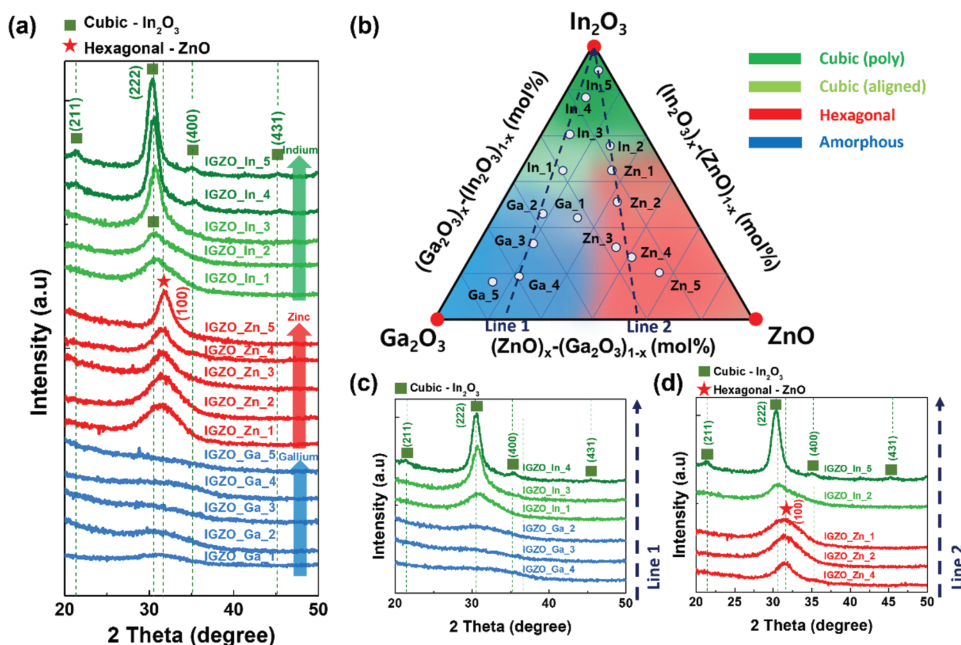

Figure 3. a) X-ray diffraction (XRD) patterns of the PEALD IGZO regarding different composition fractions. b) Ternary metal oxide phase diagram of PEALD IGZO according to crystallinity. c,d) XRD patterns with respect to line 1 (c) and line 2 (d).

solution process.[9,10] This amorphous phase was very stable; a crystalline phase did not occur even at 500 °C annealing temperature.[8] However, in our study, four cases of the crystal structure of as-deposited IGZO exhibited different XRD peak positions and intensity. We used four colors (deep green, light green, red, and blue) for each distinguishable crystal structure. The Ga-rich region (IGZO_Ga_1 to 5; $0.350 < X_{Ga} < 0.750$) was confirmed to be amorphous with no crystal peaks, as indicated by the blue color. In the Zn-rich region (IGZO_Zn_1 to 5; $0.292 < X_{Zn} < 0.633$), the hexagonal-ZnO (100) single peak was shown (JCPS card # 79-0207) as a red color. Specially, the In-rich region (IGZO_In_1 to 5; $0.535 < X_{In} < 0.917$) exhibited two different structures; for the IGZO_In_4 & 5 with a very high In fraction ($0.817 < X_{In} < 0.917$), the XRD peaks exhibited a cubic-bixbyite In_2O_3 structure with (222) peak as major and some subpeaks as minor (JCPS card # 76-0152). On the other hand, the IGZO_In_1 to 3 showed peaks of cubic-In_2O_3 (222) without other subpeaks. We separated two cases using deep green and light green, respectively. As illustrated in Figure 3b, the crystallinity of PEALD processed IGZO was mapped in a diagram using four different structure cases, and each XRD dataset is represented in Figure 3c,d for the tie-lines of L_1 and L_2. Through the XRD peaks according to L_1 and L_2, the crystal properties according to the metal composition could be reconfirmed. These two lines indicate that the crystallinity of PEALD processed IGZO is affected by the relatively dominant element, and its growth mechanism will be discussed later in this article.

To further investigate the microstructure of PEALD processed IGZO films, a high-resolution transmission electron microscopy (HR-TEM) analysis was performed using selected representative IGZO thin films with different crystal structures, as shown in **Figure 4**. The HR-TEM image with Fast Fourier transform (FFT) of the IGZO_In_4 film shows a polycrystalline cubic structure (Figure 4a). The microstructure area exhibited clear lattice fringes, and lattice plane parameters for the (222) and (400) planes of cubic-In_2O_3 structure were measured to be 0.29 and 0.25 nm, respectively.

Compared to IGZO_In_4, the TEM analysis of IGZO_In_1 with a small In content ratio showed a similar cubic structure and a lattice parameter of 0.29 nm corresponding to the (222) plane as observed in Figure 4b. The HR-TEM images according to IGZO_Zn_4 and IGZO_Zn_5 with a relatively high Zn fraction are shown in Figure 4c,f, respectively. A 0.28 nm of lattice parameter for the (100) plane of hexagonal structured ZnO was observed, and crystallinity was increased with respect to H-(100) as Zn fraction increased. For the IGZO_Ga_1 and IGZO_Ga_3, the HR-TEM images, and diffused ring-patterns of FFT indicated amorphous and nanocrystalline structures as presented in Figure 4d,e, respectively.

Here, we observed the diversity of crystal growth on PEALD processed IGZO films according to atomic composition fractions of IGZO system for both XRD and HR-TEM analyses. Since these results are exclusive compared to previous PVD processed IGZO, we need to discuss why the PEALD IGZO grows into a crystal structure. In the case of a sputtering method to grow crystallized IGZO, the semiconductor energy laboratory (SEL) reported that IGZO growth with a *c*-axis aligned crystal (CAAC) structure using an In:Ga:Zn = 1:1:1 target for deposition temperatures above 150 °C. They reported that a triangular or hexagonal shaped pellet (IGZO) was sputtered from a target and is bonded to each other through the thermal energy of substrate to grow a CAAC crystalline phase.[41,42] On the other hand, in the ALD deposition method, the precursor adsorbed on the substrate chemically reacts with the reactant. Therefore, the growth mechanism of the crystal should be different compared to the PVD method. In light of

© 2023 The Authors. Advanced Electronic Materials published by Wiley-VCH GmbH

2199160x, 0, Downloaded from https://onlinelibrary.wiley.com/doi/10.1002/aelm.202201208 by Hanyang University Library, Wiley Online Library on [09/03/2023]. See the Terms and Conditions (https://onlinelibrary.wiley.com/terms-and-conditions) on Wiley Online Library for rules of use; OA articles are governed by the applicable Creative Commons License

2199160x, 0, Downloaded from https://onlinelibrary.wiley.com/doi/10.1002/aelm.202201208 by Hanyang University Library, Wiley Online Library on [09/03/2023]. See the Terms and Conditions (https://onlinelibrary.wiley.com/terms-and-conditions) on Wiley Online Library for rules of use; OA articles are governed by the applicable Creative Commons License

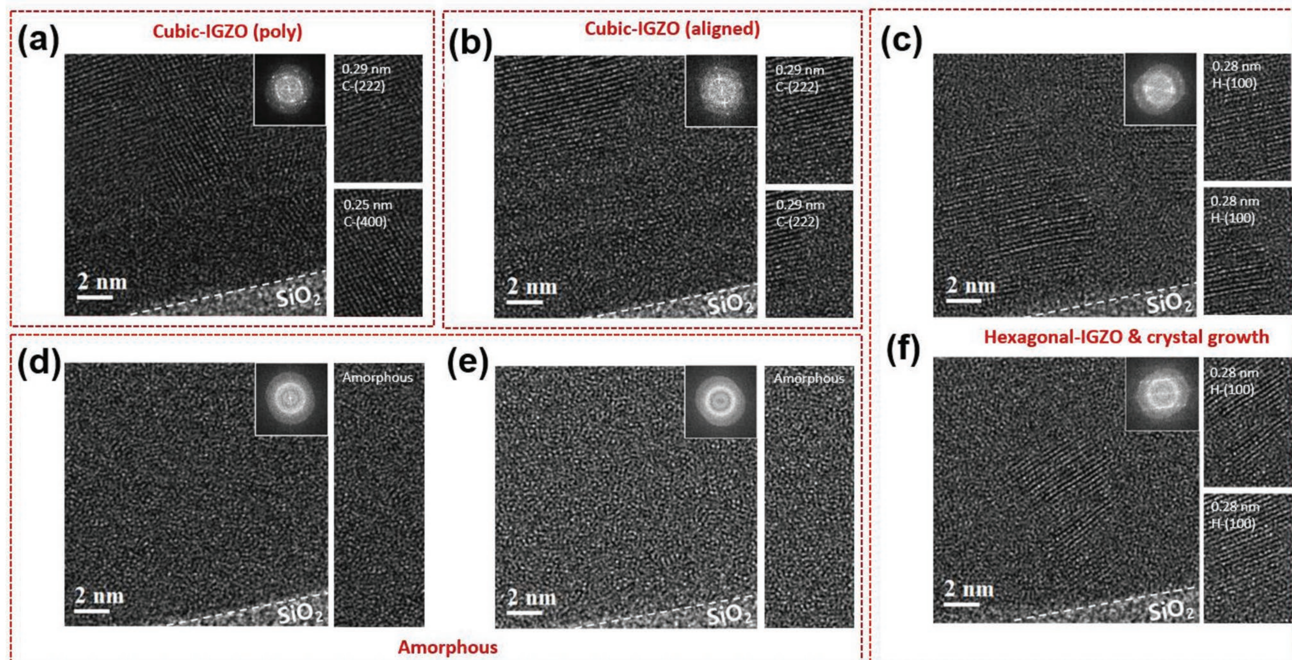

Figure 4. a–f) HR-TEM image and FFT patterns of PEALD IGZO as different composition fractions of: a) IGZO_In_4, b) IGZO_In_1, c) IGZO_Zn_4, d) IGZO_Ga_1, e) IGZO_Ga_3, and f) IGZO_Zn_5.

this, we can explain the growth mechanism of ALD processed IGZO layer: (i) there is sufficient reaction energy to adjust crystal structure and (ii) the process induces crystal growth by thicker single-metal oxide substrates. In the PEALD process, there are several publications about adjusting phase structure, including metastable phases because the plasma energy could provide sufficient reaction energies for activation.[43,44] In the second one, since the sequential ALD technique is used to deposit IGZO, the corresponding layer required to deposit a thin film in which one element dominates (such as In-rich, Ga-rich, and Zn-rich) is inevitably thick. Each layer can induce distinctive crystal growth during the ALD process because of its different surface properties, such as crystal structure and lattice planes.[45,46] We speculated that these two characteristics of PEALD can induce crystal growth according to the dominant metal oxide during the growth process of the IGZO thin film.

To investigate the effect of composition of PEALD IGZO on the characteristics of TFTs, we fabricated TFTs with bottom-gate and top-contact (shown in **Figure 5**g), and the representative transfer curves and device characteristics are summarized in Figure S4 and Table S2 (Supporting Information). The field-effect mobility (μ_{FE}), threshold voltage (V_{th}), and subthreshold swing (SS) were extracted as representative transfer characteristics of the IGZO TFTs, and each property is marked on the ternary oxide diagram, as presented in Figure 5a–c. By briefly overviewing each characteristic, the μ_{FE} shows the optimized values in a specific composition region, and the V_{th} showed a drastic negative shift in the In-rich region, and the SS values were degraded in the region the closer to the end of each single metal composition.

To interpret in more detail, we discuss comprehensively the changes of device characteristics as well as crystal structure in terms of the chemical composition ratio. We matched overlapping the crystal properties and device characteristics on the ternary oxide diagram, as shown in Figure 5d. As an example, the electrical characteristics of L_1 (In:Ga:Zn = x:3.3:1.0) and L_2 (In:Ga:Zn = y:1.0:1.7) described above are presented in Figure 5e,f. In the case of L_1, the μ_{FE} shows an extremely low value (<1 $\mathrm{cm^2\ V^{-1}\ s^{-1}}$) due to lower carrier concentration at the low concentration of In. With increasing In-fraction, the μ_{FE} steadily increases and the SS improves, and the optimal device characteristics are exhibited at an 0.53 of X_{In} (μ_{FE} = 23.6 $\mathrm{cm^2\ V^{-1}\ s^{-1}}$, SS = 0.29 V $\mathrm{decade^{-1}}$, V_{th} = 0.5 V). If the In content is increased beyond that point, the device starts to deteriorate rapidly with increased SS and a negative shift in V_{th}. This phenomenon can be explained by understanding N_{e} and crystallinity. The negative shifts of V_{th} could be explained by the increased N_{e} correlated with In fraction. Conversely, as the X_{Ga} increases, N_{e} decreases rapidly as shown in Figure 2b, and V_{th} is observed in positive shifted. IGZO_Ga_5, which has the highest X_{Ga}, did not even show transfer behavior. In the deep green region, deterioration of these device characteristics may begin due to the polycrystalline structure with grain boundaries that could cause a defect state. In the case of L_2, the μ_{FE} increased in accordance with the increase in carriers (similar to L_1) as the X_{In} increases from 0.20 to 0.63 (red region to light green region). Furthermore, in the deep green region, device degradation was observed as in L_1. Although the optimal point of each L_1 and L_2 are located in the same light green region, the device properties of L_2 have higher μ_{FE} because of the higher N_{e} due to a lower Ga fraction. The optimized TFT performance for L_2 was 43.7 $\mathrm{cm^2\ V^{-1}\ s^{-1}}$ for μ_{FE}, 0.25 for SS, and −1.1 V for V_{th}.

 © 2023 The Authors. Advanced Electronic Materials published by Wiley-VCH GmbH

2199160x, 0, Downloaded from https://onlinelibrary.wiley.com/doi/10.1002/aelm.202201208 by Hanyang University Library, Wiley Online Library on [09/03/2023]. See the Terms and Conditions (https://onlinelibrary.wiley.com/terms-and-conditions) on Wiley Online Library for rules of use; OA articles are governed by the applicable Creative Commons License

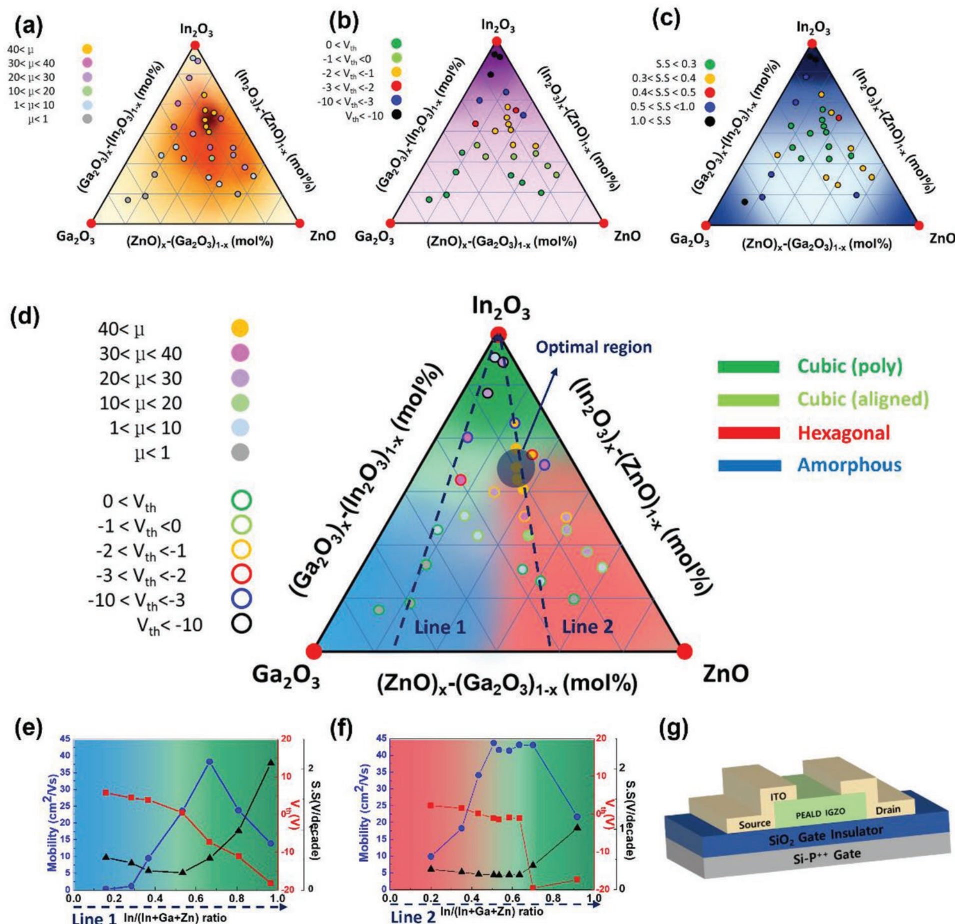

Figure 5. a–c) Ternary metal oxide phase diagram of PEALD IGZO with respect to device parameters such as: a) field-effect mobility (μ_{FE}), b) threshold voltage (V_{th}), and c) subthreshold swing (SS). d) The comprehensive ternary phase diagram of IGZO reflecting crystallinity, μ_{FE}, and V_{th}. e,f) The device characteristics according to line 1 (e) and line 2 (f). g) The device structure of the thin-film transistor (TFT) using PEALD IGZO as an active layer.

In addition, the positive bias temperature stability (PBTS, under a gate bias of V_{GS} = +20 V for the time of 3600 s at a temperature of 60 °C) was conducted for the representatives of PEALD processed IGZO TFT in **Figure 6**. Ga_4 and Zn_5 represent Ga-rich and Zn-rich compositions, respectively (In-rich was precluded because V_{th} was negatively shift more than −3 V). Ga_1 and Zn_3 were chosen because they are close to In:Ga:Z = 1:1:1. Furthermore, In_1, In_2, Zn_1, and Zn_2 were selected to represent a high-mobility device while V_{th} is close to 0. The PBTS instability mechanism in IGZO TFTs can be explained by defect creation and electron charge trapping.[47] The defect creation is typically related to degradation of SS; however, there is no significant variation of SS during PBTS stress all the sample.

In terms of composition fraction, Ga_4 and Zn_5, which are high in Zn and Ga, have poor stability, suggesting that there are many defect sites. Since the SS values of both Ga_4 and Zn_5 were higher than 0.5, this behavior is well explained with device characteristics.[47,48] Although each In, Ga, and Zn composition has an appropriate ratio in the remaining samples, the reliability of Ga_1 and Zn_3 is still poor. Each In, Ga, and Zn element has been reported that has different oxygen bonding, which could affect reliability due to oxygen-related defects; each metal–O dissociation energy has different (Zn–O; <250 kJ mol^{-1}, In–O; 346 kJ mol^{-1}, Ga–O; 374 kJ mol^{-1}).[49,50] From this point of view, the deterioration of the reliability in zinc-rich is well explained. However, to explain the whole region, a more comprehensive perspective is needed because PEALD IGZO has a crystallinity different from conventional IGZO. Since the metal composition ratio and crystallinity alter the film density, which could affect the reliability of the device, we examined the film density of the representative sample using XRR analysis (Figure S5, Supporting Information).

Thin-film density should be comprehensively understood because it is affected by both the composition ratio of each metal and by the crystalline phase. As the near amorphous phase samples, Ga_4 and Ga_1 had relatively lower densities (5.40 and 5.76 g cm^{-3}). Samples of Zn_3 (5.83 g cm^{-3}) and Zn_5 (5.94 g cm^{-3}) had relatively higher density compared to Ga_4 and Ga_1 due to its crystallinity. However, it was lower than In_1, In_2, Zn_1, and Zn_2 (6.90, 6.95, 6.83, and 6.85 g cm^{-3}, respectively). Since the In_2O_3 film density (7.18 g cm^{-3}) was higher than Ga_2O_3 (6.44 g cm^{-3}) and ZnO (5.61 g cm^{-3}), the high film density close to 7 g cm^{-3} was probably due to the

© 2023 The Authors. Advanced Electronic Materials published by Wiley-VCH GmbH

ADVANCED ELECTRONIC MATERIALS
Open Access
www.advelectronicmat.de

2199160x, 0, Downloaded from https://onlinelibrary.wiley.com/doi/10.1002/aelm.202201208 by Hanyang University Library, Wiley Online Library on [09/03/2023]. See the Terms and Conditions (https://onlinelibrary.wiley.com/terms-and-conditions) on Wiley Online Library for rules of use; OA articles are governed by the applicable Creative Commons License

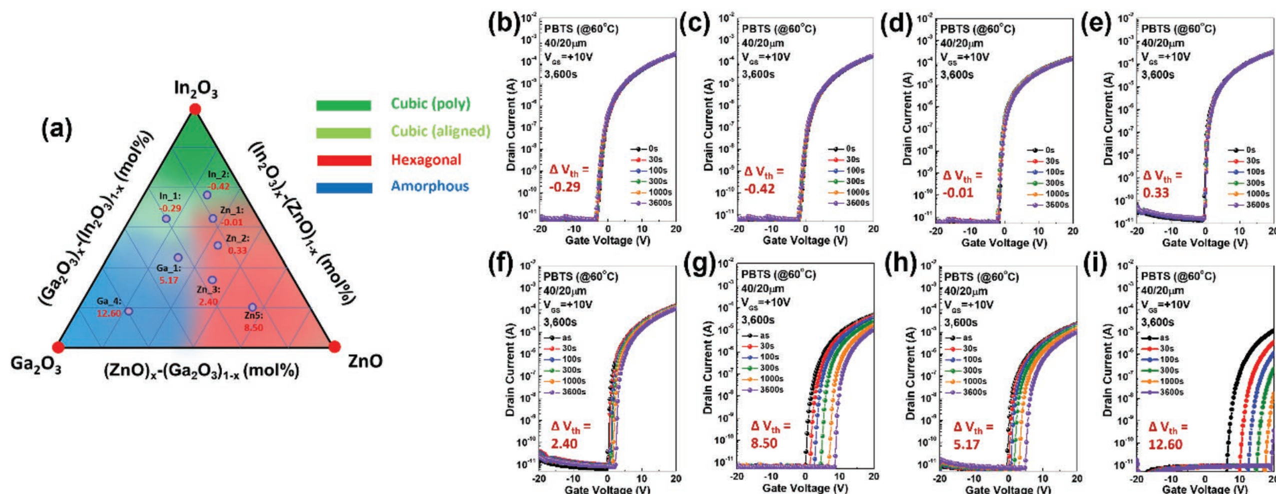

Figure 6. a) Ternary phase diagram of PEALD IGZO according to device reliability under the positive bias temperature stability (PBTS) for the time of 3600 s at a temperature of 60 °C. b–i) The representative transfer curves for PEALD-based IGZO under PBTS: b) In_1, c) In_2, d) Zn_1, e) Zn_2, f) Zn_3, g) Zn_5, h) Ga_1, and i) Ga_4.

relatively high In composition ratio. Consequently, the In_1, In_2, Zn_1, and Zn_2 exhibited high film density because of high In content within the crystalline phase.

The clockwise hysteresis characteristics are observed in only the Ga-rich region, which might be due to the relatively low density because it is related to the electron trap near the interface between the insulator and active layer. These film density properties are well explained based on the inferior PBTS behavior of Ga_1 and Zn_3, because if a compositional position is in an amorphous region or low In composition region with a relative low of film density, this could create defect states due to loose ionic binding states.[30,51] On the other hand, In_1, In_2, Zn_1, and Zn_2, which have a higher film density due to the crystal structure and high In composition, exhibited stable PBTS behavior.

Herein, we discussed the composition of IGZO grown via PEALD and its thin-film properties. Each element had a different optical, electrical, and structural role in multicomponent IGZO. The crystal structure of PEALD IGZO showed unique properties compared to previous results. Overall, we found the optimal region of IGZO for TFT performance when using the PEALD super cycle technique. The region of 0.56–0.63 for the X_{In}, 0.13–0.17 for X_{Ga}, and 0.17–0.34 for X_{Zn} was the optimal device characteristics as indicated as a circle on the ternary oxide phase diagram in Figure 5d.

3. Conclusion

To explore the metal cation composition range of the IGZO system by ALD deposition for the high mobility and robust device stability, we synthesized the IGZO films with various compositions by sequential PEALD and evaluated the microstructure, physical, and electrical properties. XPS analysis of the films deposited using the supercycle technique of PEALD exhibited a designed composition in the vertical direction and a homogeneous chemical distribution. The trends of metal composition-dependent E_g and carrier concentration of ALD processed IGZO films were similar to previous reported results, in which the role of metal cation in a multicomponent oxide system plays independent within the as-deposited film. Based on this concept, we selected chemical composition species on two tie-lines, L_1 (In:Ga:Zn = X:3.3:1.0) and L_2 (In:Ga:Zn = X:1.0:1.7), to analyze the electrical and physical properties. For the same tie line of both cases (the case of the same ratio of Ga and Zn), the carrier concentration increased with increasing In fraction. As compared to the two tie-line case (the case of the same ratio of In), the carrier concentration decreased with increasing the amount of Ga. In addition, as-deposited IGZO grown into crystal structure corresponding to the dominant metal component oxide during PEALD process.

Additionally, we fabricated TFTs using PEALD processed IGZO film as an active layer onto Si substrates to evaluate the device performance according to the change in the metal composition. Since the device characteristics could be influenced by various factors such as electrical properties, crystallinity, and defect states, they should be interpreted in light of the thin-film properties. Considering properties such as mobility and device stability under PBTS, we suggested the region of 0.56–0.63 for X_{In}, 0.13–0.17 for X_{Ga}, and 0.17–0.34 for X_{Zn}, in which the device exhibited remarkable electrical properties such as a high μ_{FE} of 41.4–43.7 cm^2 V^{-1} s^{-1}, a low SS of 0.24–0.25 V decade^{-1}, an initial V_{th} of −0.9 to −1.0 V, and a slight V_{th} shift under PBTS. From this study, we concluded that composition control of IGZO deposited using a PEALD supercycle technique has the potential to overcome the drawbacks of sputtered IGZO films, and we explored the optimum metal cation composition range of IGZO system as prepared by PEALD.

4. Experimental Section

Thin-Film Deposition: IGZO thin films were deposited on Si(100) substrates and soda-lime glass using the PEALD process.

© 2023 The Authors. Advanced Electronic Materials published by Wiley-VCH GmbH

[3-(Dimethylamino)propyl]dimethyl indium (DADI), trimethyl gallium (TMGa), and diethyl zinc (DEZ) were used as the In, Ga, and Zn precursors, respectively. The oxygen radicals generated using Ar/O_2 plasma were used to oxidize each adsorbed precursor. The chamber pressure and plasma power were held at 1.2 Torr and 300 W during plasma generation. Each thickness and refractive index exhibited an average of evaluated samples ($n \geq 6$) for each process. The reproducibility of the ALD process was confirmed with an error rate of less than 3% in three repeated statistics.

To dose sufficient precursors, precursor dose time was adjusted with regard to each precursor vapor pressure (DADI = 1.5 s, TMGa = 0.1 s, DEZ = 0.1 s). To investigate the growth behavior of each precursor under the PEALD process, the growth temperature was varied from 100 °C to 250 °C. The composition of PEALD IGZO was adjusted using supercycles consisting of {[indium precursor vapor – purge – O_2 plasma – purge] × n_1 cycles – [gallium precursor vapor – purge – O_2 plasma – purge] × n_2 cycles – [zinc precursor vapor – purge – O_2 plasma – purge] × n_3 cycles}.

TFT Fabrication and Measurement: To fabricate the staggered bottom gate IGZO TFTs, a 20 nm-thick IGZO channel layer was deposited on thermally grown SiO_2 (100 nm)/p^{++} Si substrate. The IGZO films were patterned by conventional photolithography and the wet-etching process. Indium tin oxide (ITO) with a thickness of 100 nm was deposited by radio-frequency (RF) magnetron sputtering as source and drain electrodes. Photolithography and a lift-off method were used to avoid chemical damage to the channel layer during wet-etching of ITO. The channel layer was defined as a channel width/length (W/L) of 40/20 µm. The devices were annealed at 400 °C for 3 h in an ambient atmosphere. The electrical characteristics and reliability of the TFTs were evaluated using a Keithley 4200 semiconductor parameter analyzer. The electrical parameters of devices are extracted from measured devices ($n \geq 10$) in vacuum conditions (≈15 mTorr) at room temperature. PBTS was analyzed under a gate bias (V_{GS}) of 20 V at a temperature of 60 °C with a stress time of 3600 s, which was average from evaluated samples ($n \geq 3$) for each device. The TFTs using statistics were chosen randomly in a 2.5 × 2.5 (cm^2) sample size. The reproducibility of the device performance was confirmed with an error rate of less than 8% regarding to mobility in three repeated statistics.

Characterization: A spectroscopic ellipsometer (SE; Ellipso Technology, UV-FMS) was used to measure the thickness and refractive index of IGZO thin films. UV–visible spectroscopy was used to investigate the transmittance and bandgaps. The crystallinity of films was investigated by grazing incidence XRD (GIXRD, SmartLab, Rigaku Co) using a Cu Kα X-ray source (the crystallinity of each single metal oxide, such as In_2O_3, Ga_2O_3, and ZnO, was investigated in Figure S2, Supporting Information). The film density was analyzed by high-resolution X-ray reflectivity (XRR, SmartLab, Rigaku Co). In addition, the microstructures of IGZO thin films were analyzed using TEM (NEOARM, JEOL). The chemical composition of the IGZO films was analyzed by X-ray photoelectron spectroscopy (XPS, K-alpha+, Thermo Fisher Scientific Co) using a monochromatic Al Kα source (C 1s signals were presented in Figure S3a, Supporting Information). Hall measurements (Ecopia) were conducted to measure the electrical properties related to carrier concentration.

Supporting Information

Supporting Information is available from the Wiley Online Library or from the author.

Acknowledgements

This research was supported by the research fund of the Samsung Display OLED Center Program.

Conflict of Interest

The authors declare no conflict of interest.

Data Availability Statement

The data that support the findings of this study are available from the corresponding author upon reasonable request.

Keywords

chemical composition fraction, crystallinity, indium gallium zinc oxide (IGZO), plasma-enhanced atomic layer deposition (PEALD), thin-film transistors (TFT)

Received: November 5, 2022
Revised: December 4, 2022
Published online:

[1] K. Nomura, H. Ohta, A. Takagi, T. Kamiya, M. Hirano, H. Hosono, *Nature* **2004**, *432*, 488.
[2] J. S. Koo, D. H. Lee, S. J. Yun, W. C. Jeong, J. Y. Park, J. W. Kim, *Proc. Int. Disp. Work* **2017**, *1*, 439.
[3] H. Han, S. Jang, D. Kim, T. Kim, H. Cho, H. Shin, C. Choi, *Electronics* **2022**, *11*, 53.
[4] T. Nakagawa, Y. Negoro, S. Yoneda, H. Shishido, H. Kobayashi, M. Oota, T. Kawata, T. Ikeda, S. Yamazaki, *Jpn. J. Appl. Phys.* **2020**, *59*, SGGE01.
[5] C. M. Hsu, W. C. Tzou, C. F. Yang, Y. J. Liou, *Materials* **2015**, *8*, 2769.
[6] Y. S. Lee, Z. M. Dai, C. I. Lin, H. C. Lin, *Ceram. Int.* **2012**, *38*, S595.
[7] A. Olziersky, P. Barquinha, A. Vilà, C. Magana, E. Fortunato, J. R. Morante, R. Martins, *Mater. Chem. Phys.* **2011**, *131*, 512.
[8] P. Barquinha, L. Pereira, G. Gonçalves, R. Martins, E. Fortunato, *J. Electrochem. Soc.* **2009**, *156*, H161.
[9] W. Xu, L. Hu, C. Zhao, L. Zhang, D. Zhu, P. Cao, W. Liu, S. Han, X. Liu, F. Jia, Y. Zeng, Y. Lu, *Appl. Surf. Sci.* **2018**, *455*, 554.
[10] M. Moreira, E. Carlos, C. Dias, J. Deuermeier, M. Pereira, P. Barquinha, R. Branquinho, R. Martins, E. Fortunato, *Nanomaterials* **2019**, *9*, 1273.
[11] K. Nomura, A. Takagi, T. Kamiya, H. Ohta, M. Hirano, H. Hosono, *Jpn. J. Appl. Phys., Part 1* **2006**, *45*, 4303.
[12] G. Goṇalves, P. Barquinha, L. Pereira, N. Franco, E. Alves, R. Martins, E. Fortunato, *Electrochem. Solid-State Lett.* **2009**, *13*, H20.
[13] T. Kamiya, H. Hosono, *NPG Asia Mater.* **2010**, *2*, 15.
[14] J. Kim, J. Park, G. Yoon, A. Khushabu, J. S. Kim, S. Pae, E. C. Cho, J. Yi, *Mater. Sci. Semicond. Process.* **2020**, *120*, 105264.
[15] R. Yao, Z. Zheng, M. Xiong, X. Zhang, X. Li, H. Ning, Z. Fang, W. Xie, X. Lu, J. Peng, *Appl. Phys. Lett.* **2018**, *112*, 103503.
[16] K. Takenaka, M. Endo, G. Uchida, A. Ebe, Y. Setsuhara, *J. Alloys Compd.* **2019**, *772*, 642.
[17] S. Hong, S. Lee, M. Mativenga, J. Jang, *IEEE Electron Device Lett.* **2014**, *35*, 93.
[18] M. M. Billah, A. B. Siddik, J. B. Kim, D. K. Yim, S. Y. Choi, J. Liu, D. Severin, M. Hanika, M. Bender, J. Jang, *Adv. Electron. Mater.* **2021**, *7*, 2000896.
[19] J. He, G. Li, Y. Lv, C. Wang, C. Liu, J. Li, D. Flandre, H. Chen, T. Guo, L. Liao, *Adv. Electron. Mater.* **2019**, *5*, 1900125.
[20] H. R. Kim, M. Furuta, S. M. Yoon, *ACS Appl. Electron. Mater.* **2019**, *1*, 2363.

© 2023 The Authors. Advanced Electronic Materials published by Wiley-VCH GmbH

2199160x, 0, Downloaded from https://onlinelibrary.wiley.com/doi/10.1002/aelm.202201208 by Hanyang University Library, Wiley Online Library on [09/03/2023]. See the Terms and Conditions (https://onlinelibrary.wiley.com/terms-and-conditions) on Wiley Online Library for rules of use; OA articles are governed by the applicable Creative Commons License

[21] S. Choi, B. Kim, J. K. Jeong, Y. H. Song, *IEEE Trans. Electron Devices* **2019**, *66*, 4739.
[22] H.-R. Kim, J.-H. Yang, G.-H. Kim, S.-M. Yoon, *J. Vac. Sci. Technol., B* **2019**, *37*, 010602.
[23] T. Hong, K. Kim, S. H. Choi, S. H. Lee, K. L. Han, J. H. Lim, J. S. Park, *ACS Appl. Electron. Mater.* **2022**, *4*, 3010.
[24] J. Sheng, H. J. Lee, S. Oh, J. S. Park, *ACS Appl. Mater. Interfaces* **2016**, *8*, 33821.
[25] J. Sheng, E. J. Park, B. Shong, J. S. Park, *ACS Appl. Mater. Interfaces* **2017**, *9*, 23934.
[26] S. M. Yoon, N. J. Seong, K. Choi, G. H. Seo, W. C. Shin, *ACS Appl. Mater. Interfaces* **2017**, *9*, 22676.
[27] M. H. Cho, H. Seol, A. Song, S. Choi, Y. Song, P. S. Yun, K. B. Chung, J. U. Bae, K. S. Park, J. K. Jeong, *IEEE Trans. Electron Devices* **2019**, *66*, 1783.
[28] M. H. Cho, M. J. Kim, H. Seul, P. S. Yun, J. U. Bae, K. S. Park, J. K. Jeong, *J. Inf. Disp.* **2019**, *20*, 73.
[29] T. H. Hong, H. J. Jeong, H. M. Lee, S. H. Choi, J. H. Lim, J. S. Park, *ACS Appl. Mater. Interfaces* **2021**, *13*, 28493.
[30] J. Sheng, T. H. Hong, H. M. Lee, K. R. Kim, M. Sasase, J. Kim, H. Hosono, J. S. Park, *ACS Appl. Mater. Interfaces* **2019**, *11*, 40300.
[31] K. M. Niang, P. M. C. Barquinha, R. F. P. Martins, B. Cobb, M. J. Powell, A. J. Flewitt, *Appl. Phys. Lett.* **2016**, *108*, 093505.
[32] W. J. Maeng, D. won Choi, J. J. S. Park, J. J. S. Park, *Ceram. Int.* **2015**, *41*, 10782.
[33] S. H. Choi, T. H. Hong, S. H. Ryu, J. S. Park, *Ceram. Int.* **2022**, *48*, 27807.
[34] D. J. Comstock, W. Elam, *Chem. Mater.* **2012**, *24*, 4011.
[35] A. Mahmoodinezhad, C. Janowitz, F. Naumann, P. Plate, H. Gargouri, K. Henkel, D. Schmeißer, J. I. Flege, *J. Vac. Sci. Technol., A* **2020**, *38*, 022404.
[36] I. Donmez, C. Ozgit-Akgun, N. Biyikli, *J. Vac. Sci. Technol., A* **2013**, *31*, 01A110.
[37] P. C. Rowlette, C. G. Allen, O. B. Bromley, A. E. Dubetz, C. A. Wolden, *Chem. Vap. Deposition* **2009**, *15*, 15.
[38] D. Kim, H. Kang, J. M. Kim, H. Kim, *Appl. Surf. Sci.* **2011**, *257*, 3776.
[39] T. Muneshwar, G. Shoute, D. Barlage, K. Cadien, *J. Vac. Sci. Technol., A* **2016**, *34*, 050605.
[40] A. Wang, T. Chen, S. Lu, Z. Wu, Y. Li, H. Chen, Y. Wang, *Nanoscale Res. Lett.* **2015**, *10*, 75.
[41] S. Yamazaki, in *Fifth Asia Symposium on Quality Electronic Design (ASQED 2013)*, IEEE, Piscataway, NJ, USA **2013**, https://doi.org/10.1109/ASQED.2013.6643553.
[42] S. Yamazaki, T. Hirohashi, M. Takahashi, S. Adachi, M. Tsubuku, J. Koezuka, K. Okazaki, Y. Kanzak, H. Matsukizono, S. Kaneko, S. Mori, T. Matsuo, *J. Soc. Info. Disp.* **2014**, *1*, 55.
[43] V. D. Wheeler, N. Nepal, D. R. Boris, S. B. Qadri, L. O. Nyakiti, A. Lang, A. Koehler, G. Foster, S. G. Walton, C. R. Eddy, D. J. Meyer, *Chem. Mater.* **2020**, *32*, 1140.
[44] M. Ziegler, S. Yüksel, S. Goerke, K. Weber, D. Cialla-May, J. Popp, K. Pollok, D. Wang, F. Langenhorst, U. Hübner, P. Schaaf, H. G. Meyer, *Adv. Mater. Technol.* **2017**, *2*, 1700015.
[45] M. Coll, M. Napari, *APL Mater.* **2019**, *7*, 110901.
[46] H. C. M. Knoops, T. Faraz, K. Arts, W. M. M. (E.) Kessels, *J. Vac. Sci. Technol., A* **2019**, *37*, 030902.
[47] J. Sheng, T. Hong, D. Kang, Y. Yi, J. H. Lim, J. S. Park, *ACS Appl. Mater. Interfaces* **2019**, *11*, 12683.
[48] I. H. Baek, J. J. Pyeon, S. H. Han, G. Y. Lee, B. J. Choi, J. H. Han, T. M. Chung, C. S. Hwang, S. K. Kim, *ACS Appl. Mater. Interfaces* **2019**, *11*, 14892.
[49] N. Saito, T. Ueda, T. Tezuka, K. Ikeda, *IEEE J. Electron Devices Soc.* **2018**, *6*, 1258.
[50] H. W. Park, J. Bae, H. Kang, D. H. Kim, P. Jung, H. Park, S. Lee, J. U. Bae, S. Y. Yoon, I. Kang, *Dig. Tech. Pap. – SID Int. Symp.* **2019**, *50*, 1222.
[51] H. J. Yang, H. J. Seul, M. J. Kim, Y. Kim, H. C. Cho, M. H. Cho, Y. H. Song, H. Yang, J. K. Jeong, *ACS Appl. Mater. Interfaces* **2020**, *12*, 52937.

© 2023 The Authors. Advanced Electronic Materials published by Wiley-VCH GmbH

2199160x, 0, Downloaded from https://onlinelibrary.wiley.com/doi/10.1002/aelm.202201208 by Hanyang University Library, Wiley Online Library on [09/03/2023]. See the Terms and Conditions (https://onlinelibrary.wiley.com/terms-and-conditions) on Wiley Online Library for rules of use; OA articles are governed by the applicable Creative Commons License